Superconducting topological Dirac semimetals: $P6/m$-Si_6 and $P6/m$-$NaSi_6$

Alex Taekyung Lee*
Department of Applied Physics, Yale University, New Haven, Connecticut 06520, USA

Kyungwha Park
Department of Physics, Virginia Tech, Blacksburg, Virginia 24061, USA

In-Ho Lee†
Korea Research Institute of Standards and Science, Daejeon 34113, Korea

(Received 3 May 2022; revised 19 February 2023; accepted 22 February 2023; published 13 March 2023)

We theoretically propose that hexagonal silicon-based crystals $P6/m$-Si_6 and $P6/m$-$NaSi_6$ are topological Dirac semimetals with superconducting critical temperatures of 12 K and 13 K, respectively, at ambient pressure. Band inversion occurs with the Fu-Kane topological invariant $\mathbb{Z}_2 = 1$, even in the absence of spin-orbit coupling. The Dirac nodes protected by C_6 crystal rotational symmetry remain gapless with spin-orbit coupling. Using first-principles calculations, we find pressure-induced topological phase transitions for $P6/m$-Si_6 and $P6/m$-$NaSi_6$ with critical external pressures of 11.5 GPa and 14.9 GPa, respectively. Above the critical pressures, the Dirac bands are gapped with $\mathbb{Z}_2 = 0$, while the superconducting states and the crystal symmetries are retained. Our results may shed light into a search for silicon-based topological materials with superconductivity.

DOI: 10.1103/PhysRevB.107.115127

I. INTRODUCTION

Semiconducting silicon becomes indispensable in electronics due to its versatile features such as the ease of electron or hole doping in a wide range, high-temperature stability, nontoxicity, and natural abundance. It is not uncommon to modify phases of solids by varying crystal structures and/or applying external stimuli. There has been a great effort in fabricating silicon in different condensed matter phases, especially a superconducting phase. Some metallic silicon phases were proposed to be superconducting under high pressures [1–5]. For doped silicon clathrates and boron-doped cubic silicon, superconductivity was observed at ambient pressure [6–8]. Recently, hexagonal silicon-based crystals $P6/m$-Si_6 and $P6/m$-$NaSi_6$, which can be synthesized similarly to Ref. [9], were predicted to show superconductivity (transition temperature of 12 K and 13 K, respectively) at ambient pressure [10].

Topology in the reciprocal space plays an important role in quantum materials properties due to topological protection. Based on symmetries, gapped and gapless quantum phases including a superconducting phase can be topologically classified [11]. For example, three-dimensional Dirac semimetals which can exist in the presence of time-reversal and inversion symmetries, are categorized into two classes [12]. In the first class, band inversion occurs with a nontrivial Fu-Kane $\mathbb{Z}_2$ topological invariant [13] and associated Fermi arc surface states, and Dirac nodes are protected by crystal rotational symmetry [14,15]. This class is henceforth referred to as a topological Dirac semimetal phase, following Ref. [12]. In the second class, Dirac nodes are protected by nonsymmorphic space group [16] without band inversion.

Most topological materials are not based on silicon. A topological Dirac semimetal phase was discovered in a silicon-containing compound $CaAl_2Si_2$ (space group No. 164, point group D_{3d}) [17,18] in the presence of spin-orbit coupling (SOC). Silicon-based crystals *Cmcm*-AHT-Si_{24} and *Cmcm*-VFI-Si_{36} have been proposed to be topological nodal line semimetals *only* when SOC is excluded [19]. With SOC, the nodal lines are gapped with a small energy gap of 1 meV [19].

Recently, superconductivity was observed in three-dimensional topological Dirac semimetals such as Cd_3As_2 [20–22], Au_2Pb [23,24], KZnBi [25], $PdTe_2$ [26,27], and $BaSn_3$ [28]. To the best of our knowledge, silicon-based topological Dirac semimetals with superconductivity have not been proposed or synthesized yet. Superconductivity in topological Dirac semimetals is appealing considering the possibility to create odd-parity or spin-triplet Cooper pair interaction by doping and/or breaking time-reversal symmetry [29–31]. Furthermore, superconductors with a nontrivial Fu-Kane $\mathbb{Z}_2$ topological invariant were proposed to be platforms for realization of Majorana zero modes [32] whose braiding is used for topological quantum computation [33,34]. Families of superconductors with a nontrivial $\mathbb{Z}_2$ invariant showed promising experimental signatures of Majorana zero modes at the ends of magnetic vortices [35,36].

In this work, we propose that $P6/m$-Si_6 and $P6/m$-$NaSi_6$ are topological Dirac semimetals with superconductivity at ambient pressure even when SOC is included. We find that the silicon-based crystals undergo a topological phase transition driven by hydrostatic pressure without any structural changes. Above slightly different critical pressures, both silicon-based

*neotechlee@gmail.com
†Corresponding author: ihlee@kriss.re.kr

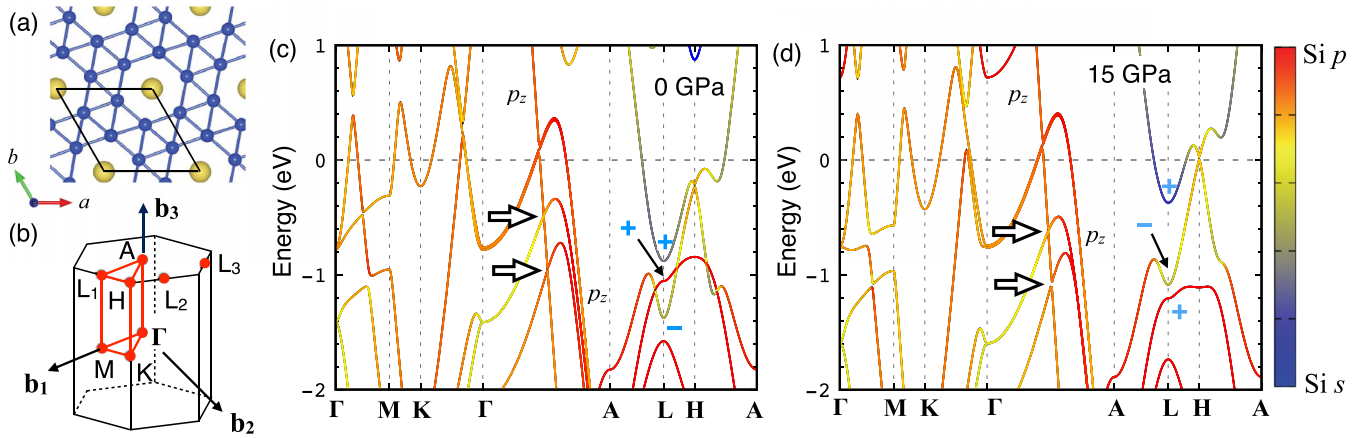

FIG. 1. (a) Top view of the atomic structure of $P6/m$-$NaSi_6$ with a unit cell. Isostructure $P6/m$-Si_6 can be obtained by removing Na atoms from $P6/m$-$NaSi_6$. (b) First Brillouin zone for $P6/m$-Si_6 and $P6/m$-$NaSi_6$. SOC-included DFT band structures of $P6/m$-Si_6 at (c) 0 GPa and (d) 15 GPa, where the Fermi level is set to zero. All bands are at least doubly degenerate. Relative proportions of Si s- and p-orbital characters are encoded in colors. The Dirac points are indicated as arrows and the parity of a few occupied bands are shown.

crystals become topologically trivial in the superconducting state.

II. METHODS

We employ density functional theory (DFT) with projector augmented wave (PAW) [37] pseudopotentials and the Perdew-Burke-Ernzerhof generalized gradient approximation (PBE-GGA) [38] for the exchange-correlation functional, as implemented in the VASP software [39]. A plane-wave basis set with a kinetic energy cutoff of 500 eV is used. We use Γ-centered **k**-point meshes of $8 \times 8 \times 20$ for bulk $P6/m$-Si_6 and $P6/m$-$NaSi_6$ and $8 \times 8 \times 1$ for finite slabs. Starting with the geometries from Ref. [10], we further optimize the atomic coordinates and lattice constants until the residual forces are less than 0.01 eV/Å with and without pressure. The optimized bulk hexagonal lattice parameters for $P6/m$-Si_6 ($P6/m$-$NaSi_6$) are $a = 6.81$ (6.76) Å and $c = 2.50$ (2.44) Å without pressure, which are close to those in Ref. [10]. The relaxed atomic coordinates can be found in Appendix A (see Fig. 8 and Table II.).

We compute the Fu-Kane $\mathbb{Z}_2$ topological invariant [13] from the parity of all valence or occupied bands at the time-reversal invariant momentum (TRIM) points as well as by using the Wilson loop method [40,41]. To apply the Wilson loop method and to investigate the surface states, we first construct a tight-binding Hamiltonian for the Si $s + p$ bands by generating 24 (33) maximally localized Wannier functions for $P6/m$-Si_6 ($P6/m$-$NaSi_6$), using WANNIER90 code [42] (see Appendix C: Fig. 9 and Table III). Then, we calculate the surface Green's function of the semi-infinite system based on the Wannier-function tight-binding model, using WannierTools code [41]. Irreducible representations of bands at the high symmetry **k** points and along the Γ-A axis are obtained using Quantum Espresso [43].

III. RESULTS AND DISCUSSION

The atomic structure of $P6/m$-$NaSi_6$ (space group No. 175, point group C_{6h}) is shown in Fig. 1(a), where the stacking along the c axis is identical for all atomic layers. The structure of $P6/m$-Si_6 is obtained by simply removing Na atoms from that of $P6/m$-$NaSi_6$ (see Appendix A). The Na atoms can be easily removed by the degassing process, since the migration barrier of Na atoms along the cylindrical holes is only 0.48 eV [10]. This barrier is 0.17 eV lower than that for the $Cmcm$ phase [9].

Let us first discuss electronic and topological properties without pressure and then with pressure. Figure 1(c) shows the electronic structure of $P6/m$-Si_6 at symmetric **k** points with SOC in the absence of pressure. Mostly p-orbital character is dominant near the Fermi level. However, s-orbital character is locally dominant in the $k_z = \pi/c$ plane, i.e., along the A-L-H-A lines. At the L point, bands at −0.86 eV and −1.04 eV (relative to the Fermi level) have strong s-orbital and p_z-orbital characters, respectively, while bands at −1.36 eV have characters of mixed s and $p_x + p_y$ orbitals (see Appendix B: Fig. 10). Strong Si p-orbital characteristics also appear in most of the **k** space except for the $k_z = \pi/c$ plane for $P6/m$-$NaSi_6$, as presented in Fig. 2.

For $P6/m$-Si_6 at 0 GPa, the parity analysis at the TRIM points gives $\mathbb{Z}_2 = 1$ (see Appendix C) which results from the band inversion at the L points, as shown in Fig. 1(c). (Note that a unit cell of $P6/m$-Si_6 has 24 valence electrons.) At the L points, the 23rd and 24th (25th and 26th) bands at −1.36 eV (−1.04 eV) have − (+) parity, as depicted in Fig. 1(c). The band inversion is not induced by SOC because $\mathbb{Z}_2 = 1$ without SOC.

The analysis of irreducible representations at the L point indicates that the opposite parity for the two band pairs originates from the horizontal mirror symmetry σ_h. The irreducible representation and eigenvalues of σ_h of the bands at the L point are listed in Table I. The 23rd/24th bands belong to irreducible representation B_u (where an eigenvalue of horizontal mirror reflection σ_h is +1), while the 25th/26th bands belong to irreducible representation B_g (where an eigenvalue of σ_h is −1). We also confirm that $\mathbb{Z}_2 = 1$ using the Wilson loop method (see Appendix C). Even when the parity of all

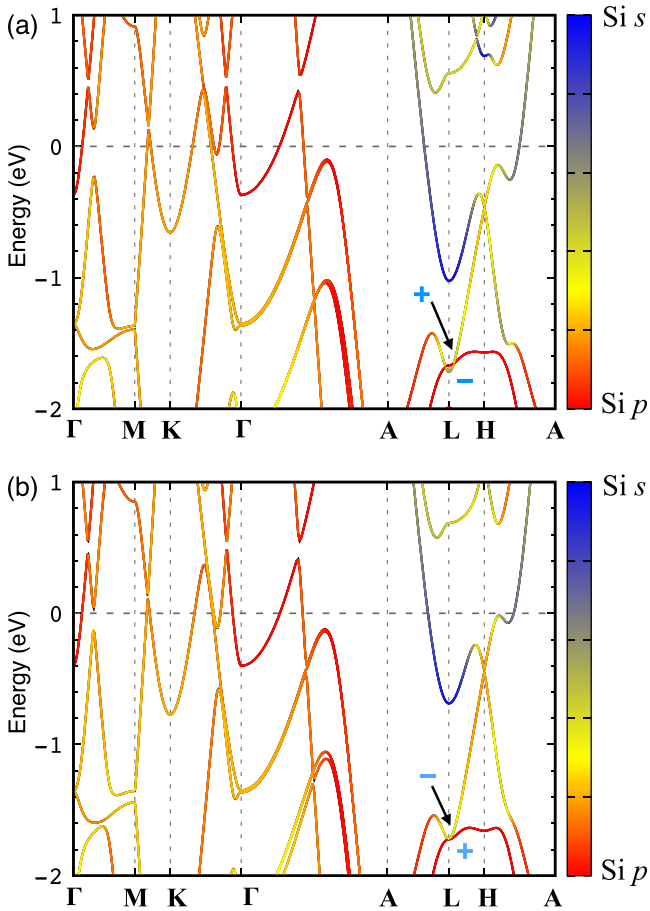

FIG. 2. Electronic band structure obtained from first-principles calculations using DFT. First-principles band structures of $P6/m$-$NaSi_6$ at pressure (a) 0 GPa and (b) 15 GPa, including spin-orbit coupling. According to the relative weight of the Si s character and the Si p character, the band color was encoded as shown in the legend. The band structure calculation at pressure 15 GPa shows the band structure just before band inversion occurs. The situation of band inversion that occurs with changes in pressure can be seen, especially in the L-H section.

occupied bands below the Fermi level is counted, we find that $\mathbb{Z}_2 = 1$ persists.

For $P6/m$-Si_6 with SOC in the absence of pressure, along the Γ-A direction, we find several possible band crossing points in the vicinity of the Fermi level. To identify gapless Dirac nodes, we zoom in the bands near the crossing points with numerical accuracy of 10 μeV, as shown in Fig. 3. The bands at i, ii, and iv are gapped with 0.07−28.9 meV, while the crossing points iii and v are gapless within numerical accuracy. We also analyze irreducible representations Λ_i of the bands near the crossing points, considering that double group C_6 is applied to the bands along the Γ-A direction. This symmetry analysis [Figs. 3(b)–3(e)] agrees with the numerical result. The Dirac nodes along the k_z axis are protected by the crystal sixfold rotational symmetry C_6. The gapless protected Dirac nodes in conjunction with our analysis of the $\mathbb{Z}_2$ invariant, suggest that $P6/m$-Si_6 is a topological Dirac semimetal.

TABLE I. Irreducible representation (irrep), point group symmetries, and their eigenvalues of bands at L point, for $P6/m$-Si_6 at 0 GPa. C_2 is two-fold rotation operator with respect to the z axis. I and σ_h are two-fold inversion and horizontal mirror plane operators, respectively. The highest occupied band is 24th band.

band #	irrep	C_2	σ_h	I
1, 2	B_u	−1	+1	−1
3, 4	A_g	+1	+1	+1
5, 6	B_g	−1	−1	+1
7, 8	B_u	−1	+1	−1
9, 10	A_u	+1	−1	−1
11, 12	A_g	+1	+1	+1
13, 14	B_g	−1	−1	+1
15, 16	A_u	+1	−1	−1
17, 18	B_u	−1	+1	−1
19, 20	A_g	+1	+1	+1
21, 22	A_u	+1	−1	−1
23, 24	B_u	−1	+1	−1
25, 26	B_g	−1	−1	+1

For $P6/m$-$NaSi_6$, it is tricky to compute the $\mathbb{Z}_2$ invariant by counting the parity of N bands at the TRIM points, where N is the number of valence electrons, since N is now an odd number due to the Na atom. (In Ref. [13], each degenerate pair was counted only once for centrosymmetric metals.) In order to circumvent this, we take into account all occupied bands below the Fermi level at the TRIM points in our calculation of the $\mathbb{Z}_2$ invariant. Note that there are different numbers of occupied bands at different TRIM points. For $P6/m$-$NaSi_6$ at 0 GPa, the product of the parity values of all occupied bands at each L point is positive, while the corresponding products at the other 5 TRIM points are negative (see Appendix C). This gives rise to $\mathbb{Z}_2 = 1$ and the band inversion also occurs at the L points, as shown in Fig. 2(a). Therefore, similarly to $P6/m$-Si_6, $P6/m$-$NaSi_6$ is also a topological Dirac semimetal.

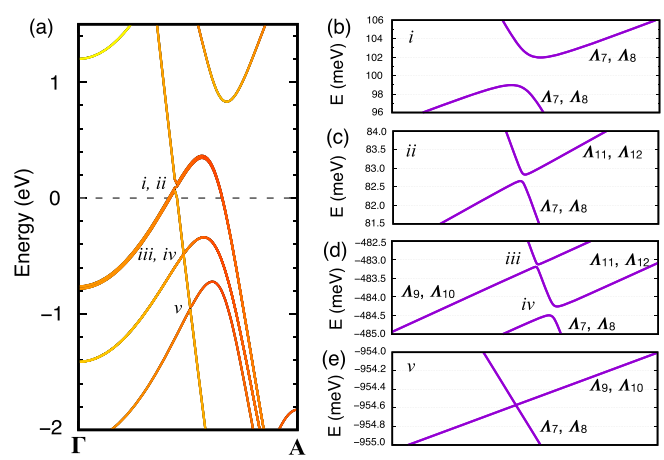

FIG. 3. SOC-included DFT bands for (a) $P6/m$-Si_6 at 0 GPa, between Γ and A. (b)-(e) enlarged bands near 5 possible band crossing points (i-v) for (a). Λ_i represent irreducible representations of double group C_6 along the Γ-A direction. Points iii and v are gapless Dirac nodes (when $\Lambda_{7,8}$ bands and $\Lambda_{9,10}$ bands meet each other).

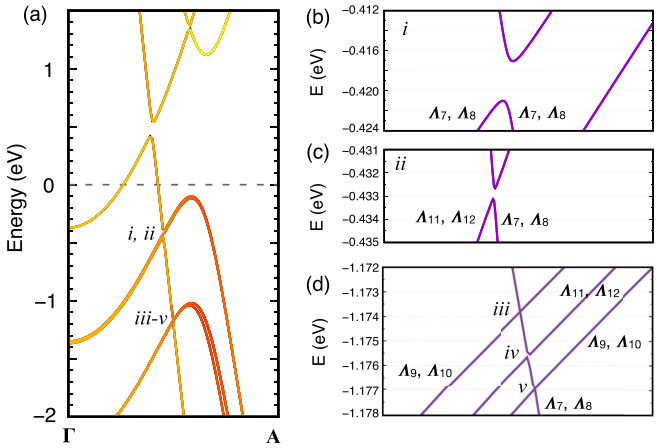

FIG. 4. (a) DFT bands in $P6/m$-$NaSi_6$ at 0 GPa, between Γ and A. (b)-(d) enlarged bands near 5 possible band crossing points (i-v) for (a). Points iii and v are gapless Dirac nodes (when $\Lambda_{7,8}$ bands and $\Lambda_{9,10}$ bands meet each other).

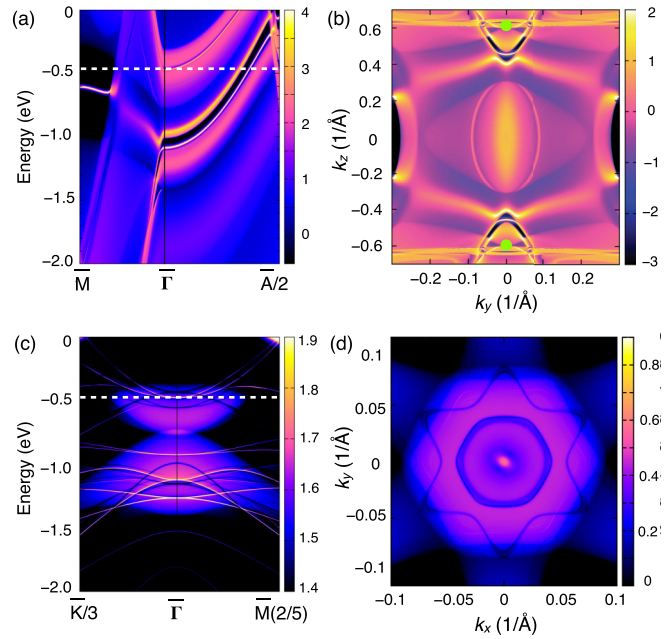

FIG. 5. Electronic structure or local density of states of surface states along the two-dimensional symmetric **k** points (a),(c), in the k_y-k_z plane (b) and in the k_x-k_y plane (d) for the semi-infinite (100) and (001) surfaces of $P6/m$-Si_6, respectively. Horizontal dashed lines in (a) and (c) represent the Dirac point energies, respectively. Filled dots in (b) represent the projection points of the Dirac nodes onto the k_y-k_z plane. In (a)-(d), bright color indicates higher density of states at the surface.

The gapless Dirac nodes [crossing points iii and v in Fig. 4(d)] are found below the Fermi level.

The nontrivial topology of three-dimensional Dirac bands in $P6/m$-Si_6 and $P6/m$-$NaSi_6$ indicates that there are nontrivial surface states. We calculate surface states using the surface Green's function of the semi-infinite system described earlier, considering two surface types: surfaces parallel and perpendicular to the Γ-A direction, i.e., (100) and (001) surfaces, respectively. Figure 5 shows the calculated local density of states which is an imaginary part of the surface Green's function, for the (100) and (001) surfaces. At the chemical potential, corresponding to one of the Dirac node energies, for the (100) surface, two arc-shaped (left and right sides of hourglass) surface states connect the two Dirac node projection points (with bulk characteristics) indicated as solid dots along the k_z axis in Fig. 5(b). This is expected because each Dirac node consists of degenerate Weyl nodes with opposite chirality in topological Dirac semimetals [14,44]. For the (001) surface, the surface states appear as a point [Fig. 5(d)]. In this case, the two Dirac nodes along the k_z axis are projected onto the same point, i.e., the origin, in the k_x-k_y plane. Thus, pointlike surface states are expected rather than arc-shaped surface states. The features of the surface states for the (100) and (001) surfaces agree with those of prototype topological Dirac semimetals Na3Bi [14] and Cd_3As_2 [15].

Now with pressure up to 15 GPa, the $P6/m$ crystal symmetry is still maintained for $P6/m$-Si_6 and $P6/m$-$NaSi_6$. Since the effect of pressure is similar for both crystals, as shown in Figs. 1 and 2, we mainly discuss $P6/m$-Si_6. At 15 GPa, the amount of changes of the band structure depends on orbital characters. Specifically, the bands of s-orbital character are sensitive to pressure, while the bands of p-orbital character are somewhat rigid [Fig. 1(d)]. The band structure near the Fermi level changes significantly only in the $k_z = \pi/c$ plane [Figs. 1(c) and 1(d)]. At the L points, the s-orbital band is shifted by 0.51 eV, whereas the highest-energy occupied p-orbital band is shifted by 0.16 eV.

While the topological invariant is insensitive to small local perturbations such as disorder or impurities, pressure-induced deformation can be used to control the electronic structure [45–48]. For $P6/m$-Si_6, under high pressure, the parity of the 23rd/24th bands is reversed to that of the 25th/26th bands at the L point [see the bands in the energy window between −1.4 and −1.0 eV in Fig. 1(d)], and so the bands with − parity become higher in energy than the bands with + parity, which removes the band inversion. This leads to a topological phase transition from nontrivial $\mathbb{Z}_2 = 1$ to trivial $\mathbb{Z}_2 = 0$. The critical external pressure for the topological phase transition in $P6/m$-Si_6 is 11.5 GPa [see Fig. 6(a)]. The gapless Dirac nodes which exist below the critical pressure now open up a gap above the critical pressure, as shown in Fig. 1(d), due to the topological phase transition. In the case of $P6/m$−$NaSi_6$, a similar topological phase transition occurs at 14.9 GPa, which is somewhat higher than the critical pressure of $P6/m$-Si_6.

Theoretically, $P6/m$-Si_6 and $P6/m$-$NaSi_6$ were proposed to be superconductors at ambient pressure [10]. Figure 6(b) shows the superconducting critical temperature T_c as a function of hydrostatic pressure. While T_c decreases monotonically as pressure (P) increases, both $P6/m$-Si_6 and $P6/m$-$NaSi_6$ are superconducting within the pressure range we consider, $0 \leqslant P \leqslant 15$ GPa. Therefore, we propose that $P6/m$-Si_6 ($P6/m$-$NaSi_6$) is a superconducting topological Dirac semimetal below 11.5 (14.9) GPa. We emphasize that $P6/m$-Si_6 and $P6/m$-$NaSi_6$ consist of light elements with atomic number 14 or less, based on silicon, in contrast to

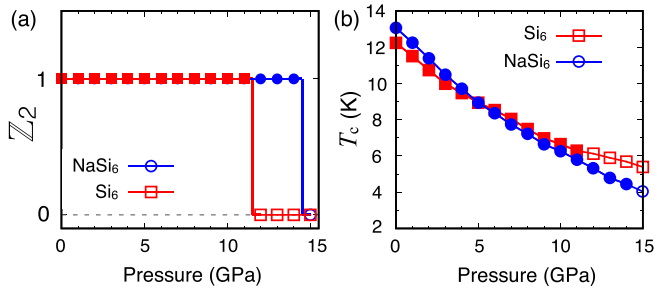

FIG. 6. (a) $\mathbb{Z}_2$ topological invariants for $P6/m$-Si_6 and $P6/m$-$NaSi_6$ are shown as a function of external hydrostatic pressure. Critical external pressures of the topological phase transitions for $P6/m$-Si_6 and $P6/m$-$NaSi_6$ are 11.5 GPa and 14.9 GPa, respectively. (b) Superconducting critical temperatures T_c of $P6/m$-Si_6 and $P6/m$-$NaSi_6$, obtained from Ref. [10] are shown as a function of external pressure. In (a) and (b), the filled (empty) symbols indicate the $\mathbb{Z}_2 = 1$ ($\mathbb{Z}_2 = 0$) phase.

reported superconducting topological Dirac semimetals such as Cd_3As_2 [20–22], Au_2Pb [23], KZnBi [25], $PdTe_2$ [26,27], and $BaSn_3$ [28] which consist of heavy elements.

Due to the nesting vectors along k_z, it turns out that there is a modulation in Si-Si bond lengths (out-of-hexagonal plane) formed in the z direction. Indeed, we found a small oscillation of the out-of-plane bond length in the slab geometry (see Appendix D: Fig. 11). The modulation is strongest on the surface and decreases near the center of the slab.

We calculated the Fermi surfaces from the two crystal structures $P6/m$-Si_6 and $P6/m$-$NaSi_6$ as presented in Fig. 7. $P6/m$-Si_6 and $P6/m$-$NaSi_6$ can provide Dirac cones near or at the Fermi energy and show an anisotropic conducting channel due to their anisotropic bonding nature. Evidence of our proposed pressure-induced topological phase transition in $P6/m$-Si_6 and $P6/m$-$NaSi_6$ may be explored by transport experiments. The three-dimensional Dirac nodes and resultant

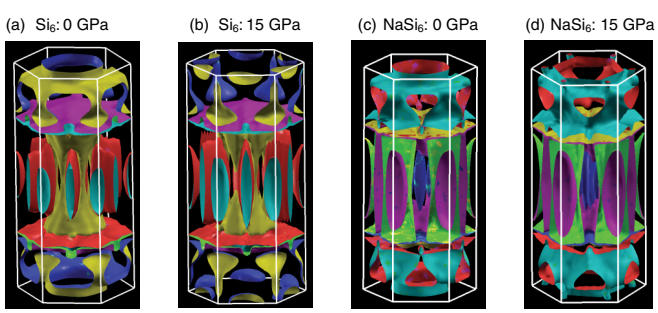

FIG. 7. Fermi surfaces of (a) $P6/m$-Si_6 at 0 GPa, (b) $P6/m$-Si_6 at 15 GPa, (c) $P6/m$-$NaSi_6$ at 0 GPa, and (d) $P6/m$-$NaSi_6$ at 150 GPa are shown, respectively. The Fermi surface is the surface of constant energy in the first BZ which separates occupied from unoccupied electron states at zero temperature. Electronic band structure obtained from first-principles calculations using DFT.

arc-shaped surface states are supposed to induce a unique field-direction dependence in Shubnikov–de Haas oscillations [49]. The chiral anomaly associated with Weyl nodes suggests the following interesting properties: (i) A large negative magnetoresistance is found when an external magnetic field is parallel to a current direction [50,51]; (ii) Thermoelectric properties depends on the relative direction between an external magnetic field and a temperature gradient [52]; (iii) The giant planar Hall effect is expected when a current direction is not parallel to a magnetic field direction in plane [53,54]. By measuring variations of the above properties upon external pressure, the proposed topological phase transition can be experimentally probed, similar to Ref. [48].

IV. CONCLUSIONS

In summary, we have proposed that $P6/m$-Si_6 and $P6/m$-$NaSi_6$ crystals are superconducting topological Dirac semimetals at ambient pressure with $\mathbb{Z}_2 = 1$. The two gapless bulk Dirac nodes appear at -0.4832 eV and -0.9546 eV for the former and at -1.1740 eV and -1.1770 eV for the latter below the Fermi level. With hole doping, the Fermi level may be lowered to one of the two Dirac node energies for experimental signatures of the topological phase. The gapless Dirac nodes are protected by the crystal rotational symmetry in the presence of time-reversal symmetry. The topological Dirac semimetal phase for the crystals becomes topologically trivial beyond a critical external pressure. This pressure-induced topological phase transition retains superconductivity and the original crystal symmetry group. The coexistence of a topological Dirac semimetal state and a superconducting state in the present crystals, along with a pressure-induced topological phase transition, will provide an interesting platform to study the interplay between topology in electronic structure and superconductivity.

ACKNOWLEDGMENTS

We thank Sohrab Ismail-Beigi for helpful discussions. This work also used the Extreme Science and Engineering Discovery Environment (XSEDE), which is supported by the National Science Foundation Grant No. ACI-1548562, by using computer time on the Comet supercomputer as enabled by XSEDE allocation No. MCA08X007. I.H.L was supported by the National Center for Materials Research Data (NCMRD) through the National Research Foundation of Korea (NRF) funded by the Ministry of Science and ICT (Grant No. NRF-2021M3A7C2089748).

APPENDIX A: ATOMIC STRUCTURE OF $P6/m$-Si_6

The crystal structure information discussed in the main text was obtained by the first-principles electronic structure calculation method.

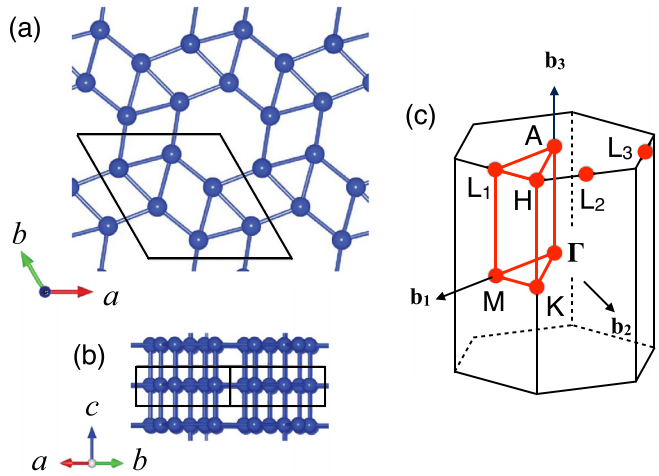

FIG. 8. (a) Top view and (b) side view of the atomic structure of $P6/m$-Si_6. $P6/m$-Si_6 can be obtained by removing Na atoms from $P6/m$-$NaSi_6$. (c) First Brillouin zone (BZ) of $P6/m$-Si_6. Γ, M, A, and L points are time-reversal invariant momentum points, which are related to $\mathbb{Z}_2$ topological invariant calculation especially for crystals with inversion symmetry. $P6/m$ (space group No. 175) is belong to the hexagonal Bravais lattice crystal system. The space group No. 175 has inversion symmetry.

APPENDIX B: BAND STRUCTURES OF $P6/m$-$NaSi_6$ AND $P6/m$-Si_6

The results of the first-principles electronic structure calculation are shown in the figure.

APPENDIX C: $\mathbb{Z}_2$ TOPOLOGICAL INVARIANT CALCULATIONS

The topological phase of band structure can be classified by calculating topological invariant. The hybrid Wannier charge center flow technique, which is equivalent to the Wilson loop method. To investigate the topological nature of the electronic states, we obtained maximally localized Wannier functions using the WANNIER90 code[55] (see Fig. 9) and performed hybrid Wannier charge center flow calculations. With this Wannier model, the symmetry properties and $\mathbb{Z}_2$ topological invariant could be directly computed. $\mathbb{Z}_2$ topological invariants were calculated by observing hybrid Wannier charge center flows. The topological surface states were calculated using the Green's function approach, as implemented in the WannierTools code [41].

TABLE III. Parities at time-reversal invariant momentum points of $P6/m$-Si_6 and $P6/m$-$NaSi_6$ at 0 GPa and 15 GPa.

		$P6/m$-Si_6		$P6/m$-$NaSi_6$	
	k-point	0 GPa	15 GPa	0 GPa	15 GPa
Γ	(0,0,0)	+	+	−	−
M_1	(0.5, 0, 0)	+	+	−	−
M_2	(0, 0.5, 0)	+	+	−	−
A	(0, 0, 0.5)	+	+	−	−
M_3	(0.5, 0.5, 0)	+	+	−	−
L_1	(0.5, 0, 0.5)	−	+	+	−
L_2	(0, 0.5, 0.5)	−	+	+	−
L_3	(0.5, 0.5, 0.5)	−	+	+	−

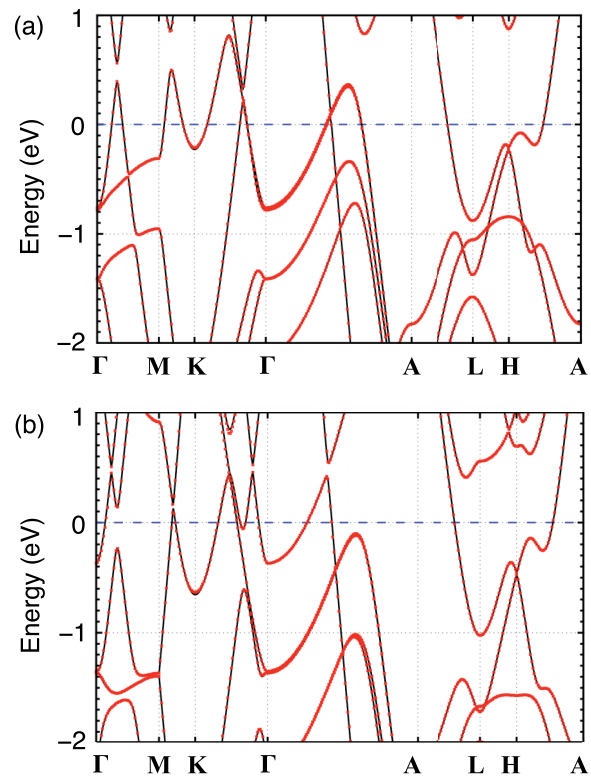

FIG. 9. First-principles bands (solid line) and Wannier bands (red filled circles) of $P6/m$-Si_6 at (a) 0 GPa and (b) 15 GPa. In the eV energy scale, there are no visible differences between two different bands. Spin-orbit coupling is included.

TABLE II. Optimized lattice parameters and atomic coordinates of $P6/m$-Si_6 and $P6/m$-$NaSi_6$ phases at external pressure (P) of 0 GPa and 15 GPa, obtained from first-principles calculations using density-functional theory (DFT). Both $P6/m$-$NaSi_6$ and $P6/m$-Si_6 phases are hexagonal with $\alpha = \beta = 90^\circ$, and $\gamma = 120^\circ$.

Material	P (GPa)	$a = b$ (Å)	c (Å)	Atom	x	y	z
$P6/m$-Si_6	0	6.813	2.501	Si (6j)	0.154	0.733	0
$P6/m$-Si_6	15	6.542	2.402	Si (6j)	0.145	0.725	0
$P6/m$-$NaSi_6$	0	6.755	2.444	Na (1b)	0	0	0.5
				Si (6j)	0.145	0.710	0
$P6/m$-$NaSi_6$	15	6.536	2.377	Na (1b)	0	0	0.5
				Si (6j)	0.144	0.713	0

TABLE IV. ν_0 and ν'_n $(n = 1, 2, 3)$ for $P6/m$-Si_6 obtained from hybrid Wannier charge center flow calculations, and corresponding $\{k_n\}$ points and **k**-planes.

k_n	k-plane	ν
k_1=0.0	k_2-k_3 plane	ν_1=1
k_1=0.5	k_2-k_3 plane	ν'_1=0
k_2=0.0	k_1-k_3 plane	ν_2=1
k_2=0.5	k_1-k_3 plane	ν'_2=0
k_3=0.0	k_1-k_2 plane	ν_3=0
k_3=0.5	k_1-k_2 plane	ν'_3=1

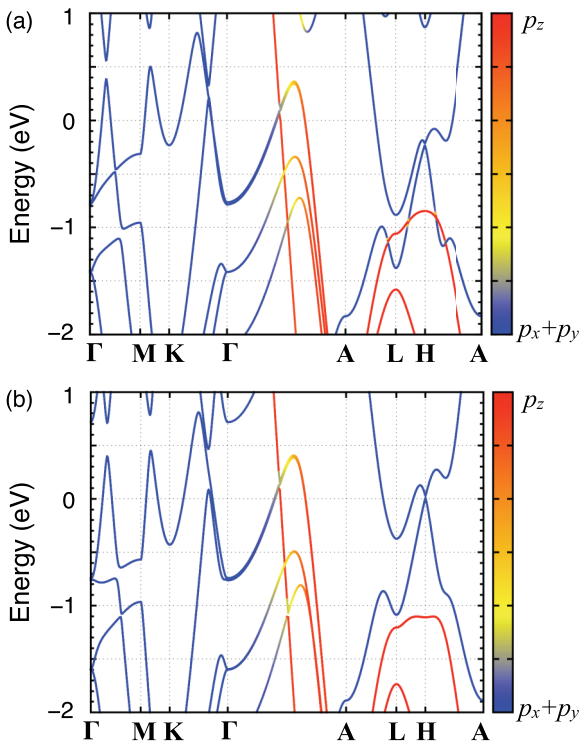

FIG. 10. Electronic band structure obtained from first-principles calculations using DFT. In the presence of SOC, band structures of $P6/m$-Si_6 at (a) 0 GPa and (b) 15 GPa and their projections on the the Si p character are shown. According to the relative weight of in-plane Si p character $(p_x + p_y)$ and out-of-plane Si p character (p_z) the band colors were encoded as shown in the legend. The situation of band inversion that occurs with changes in external pressure (>11.5 GPa) can be seen, especially in the L-H-A interval.

Space group No. 175 ($P6/m$, hexagonal) has inversion symmetry. Because of the existence of inversion symmetry in both $P6/m$-Si_6 and $P6/m$-$NaSi_6$, the Fu-Kane parity criterion can be used to easily calculate the $\mathbb{Z}_2$ topological invariants. We were able to obtain the same $\mathbb{Z}_2$ topological invariants for both $P6/m$-Si_6 and $P6/m$-$NaSi_6$ by using two different methods, observing hybrid Wannier charge center flows and investigating Fu-Kane parity criterion. ν_0 is the strong topological index. ν'_n $(n = 1, 2, 3)$ are weak topological indices. Table IV shows the example for $P6/m$-Si_6 at 0 GPa. From the hybrid Wannier charge center flow calculations, we calculated ν'_n $(n = 1, 2, 3)$. ν_0 is obtained by

$$\nu_0 = \nu_1 + \nu'_1 = \nu_2 + \nu'_2 = \nu_3 + \nu'_3 \mod 2, \tag{C1}$$

and thus we have $(\nu_0; \nu'_1\nu'_2\nu'_3) = (1; 001)$. Therefore, $P6/m$-Si_6 at 0 GPa has a strong topological nature. Similarly, we find that $P6/m$-$NaSi_6$ at 0 GPa has a strong topological nature.

APPENDIX D: Si-Si BOND LENGTHS IN THE SLAB GEOMETRY

The relaxed atomic structure of the slab structure was obtained by first-principles calculations.

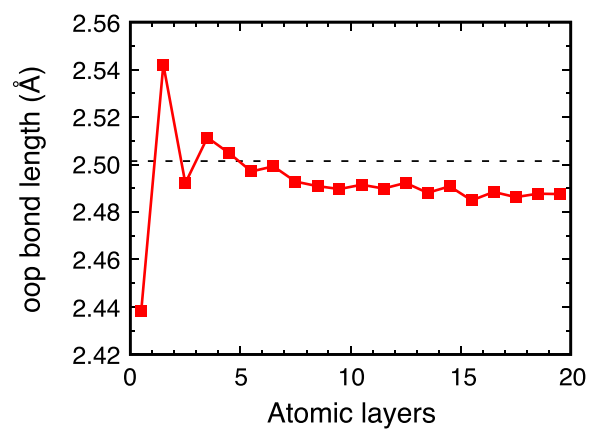

FIG. 11. Si-Si bond lengths, formed in the z direction also denoted by out-of-plane (oop bond lengths) from the hexagonal plane, in the relaxed 40-layer $P6/m$-Si_6 slab are shown. Position of the surface along the out-of-plane, is set to be zero. Dashed line represents the Si-Si bond length in the unrelaxed slab.

[1] W. Buckel and J. Wittig, Supraleitung von germanium und silizium unter hohem druck, Phys. Lett. **17**, 187 (1965).

[2] G. Stepanov, T. Valyanskaya, and E. Yakovlev, Superconductivity of metallic silicon below the pressure of transition to metallic modification, Sov. Phys. Solid State (Engl. Transl.); (United States) **22** (1980).

[3] G. Martinez, J. M. Mignot, G. Chouteau, K. J. Chang, M. M. Dacorogna, and M. L. Cohen, Superconductivity of silicon, Phys. Scr. **1986**, 226 (1986).

[4] D. Erskine, P. Y. Yu, K. J. Chang, and M. L. Cohen, Superconductivity and Phase Transitions in Compressed Si to 45 GPa, Phys. Rev. Lett. **57**, 2741 (1986).

[5] K. J. Chang, M. M. Dacorogna, M. L. Cohen, J. M. Mignot, G. Chouteau, and G. Martinez, Superconductivity in High-Pressure Metallic Phases of Si, Phys. Rev. Lett. **54**, 2375 (1985).

[6] H. Kawaji, H.-o. Horie, S. Yamanaka, and M. Ishikawa, Superconductivity in the Silicon Clathrate Compound (Na,Ba) $_x$Si$_{46}$, Phys. Rev. Lett. **74**, 1427 (1995).

[7] D. Connétable, V. Timoshevskii, B. Masenelli, J. Beille, J. Marcus, B. Barbara, A. M. Saitta, G.-M. Rignanese, P. Mélinon, S. Yamanaka, and X. Blase, Superconductivity in Doped sp^3 Semiconductors: The Case of the Clathrates, Phys. Rev. Lett. **91**, 247001 (2003).

[8] E. Bustarret, C. Marcenat, P. Achatz, J. Kačmarčik, F. Lévy, A. Huxley, L. Ortéga, E. Bourgeois, X. Blase, D. Débarre, and J. Boulmer, Superconductivity in doped cubic silicon, Nature (London) **444**, 465 (2006).

[9] D. Y. Kim, S. Stefanoski, O. O. Kurakevych, and T. A. Strobel, Synthesis of an open-framework allotrope of silicon, Nat. Mater. **14**, 169 (2015).

[10] H.-J. Sung, W. H. Han, I.-H. Lee, and K. J. Chang, Superconducting Open-Framework Allotrope of Silicon at Ambient Pressure, Phys. Rev. Lett. **120**, 157001 (2018).

[11] C.-K. Chiu, J. C. Y. Teo, A. P. Schnyder, and S. Ryu, Classification of topological quantum matter with symmetries, Rev. Mod. Phys. **88**, 035005 (2016).

[12] B.-J. Yang and N. Nagaosa, Classification of stable three-dimensional dirac semimetals with nontrivial topology, Nat. Commun. **5**, 4898 (2014).

[13] L. Fu and C. L. Kane, Topological insulators with inversion symmetry, Phys. Rev. B **76**, 045302 (2007).

[14] Z. Wang, Y. Sun, X.-Q. Chen, C. Franchini, G. Xu, H. Weng, X. Dai, and Z. Fang, Dirac semimetal and topological phase transitions in A_3bi (a = Na, k, rb), Phys. Rev. B **85**, 195320 (2012).

[15] Z. Wang, H. Weng, Q. Wu, X. Dai, and Z. Fang, Three-dimensional dirac semimetal and quantum transport in Cd_3As_2, Phys. Rev. B **88**, 125427 (2013).

[16] S. M. Young, S. Zaheer, J. C. Y. Teo, C. L. Kane, E. J. Mele, and A. M. Rappe, Dirac Semimetal in Three Dimensions, Phys. Rev. Lett. **108**, 140405 (2012).

[17] H. Su, X. Shi, W. Xia, H. Wang, X. Hanli, Z. Yu, X. Wang, Z. Zou, N. Yu, W. Zhao, G. Xu, and Y. Guo, Magnetotransport and *ab initio* calculation studies on the layered semimetal $CaAl_2Si_2$ hosting multiple nontrivial topological states, Phys. Rev. B **101**, 205138 (2020).

[18] T. Deng, C. Chen, H. Su, J. He, A. Liang, S. Cui, H. Yang, C. Wang, K. Huang, C. Jozwiak, A. Bostwick, E. Rotenberg, D. Lu, M. Hashimoto, L. Yang, Z. Liu, Y. Guo, G. Xu, Z. Liu, and Y. Chen, Electronic structure of the si-containing topological dirac semimetal $CaAl_2Si_2$, Phys. Rev. B **102**, 045106 (2020).

[19] Z. Liu, H. Xin, L. Fu, Y. Liu, T. Song, X. Cui, G. Zhao, and J. Zhao, All-silicon topological semimetals with closed nodal line, J. Phys. Chem. Lett. **10**, 244 (2019).

[20] L. Aggarwal, A. Gaurav, G. S. Thakur, Z. Haque, A. K. Ganguli, and G. Sheet, Unconventional superconductivity at mesoscopic point contacts on the 3d dirac semimetal Cd_3As_2, Nat. Mater. **15**, 32 (2016).

[21] H. Wang, H. Wang, H. Liu, H. Lu, W. Yang, S. Jia, X.-J. Liu, X. C. Xie, J. Wei, and J. Wang, Observation of superconductivity induced by a point contact on 3d dirac semimetal Cd_3As_2 crystals, Nat. Mater. **15**, 38 (2016).

[22] C. Huang, B. T. Zhou, H. Zhang, B. Yang, R. Liu, H. Wang, Y. Wan, K. Huang, Z. Liao, E. Zhang, S. Liu, Q. Deng, Y. Chen, X. Han, J. Zou, X. Lin, Z. Han, Y. Wang, K. T. Law, and F. Xiu, Proximity-induced surface superconductivity in dirac semimetal Cd_3As_2, Nat. Commun. **10**, 2217 (2019).

[23] L. M. Schoop, L. S. Xie, R. Chen, Q. D. Gibson, S. H. Lapidus, I. Kimchi, M. Hirschberger, N. Haldolaarachchige, M. N. Ali, C. A. Belvin, T. Liang, J. B. Neaton, N. P. Ong, A. Vishwanath, and R. J. Cava, Dirac metal to topological metal transition at a structural phase change in Au_2Pb and prediction of $\mathbb{Z}_2$ topology for the superconductor, Phys. Rev. B **91**, 214517 (2015).

[24] Y. Xing, H. Wang, C.-K. Li, X. Zhang, J. Liu, Y. Zhang, J. Luo, Z. Wang, Y. Wang, L. Ling, M. Tian, S. Jia, J. Feng, X.-J. Liu, J. Wei, and J. Wang, Superconductivity in topologically nontrivial material Au_2Pb, npj Quantum Mater. **1**, 16005 (2016).

[25] J. Song, S. Kim, Y. Kim, H. Fu, J. Koo, Z. Wang, G. Lee, J. Lee, S. H. Oh, J. Bang, T. Matsushita, N. Wada, H. Ikegami, J. D. Denlinger, Y. H. Lee, B. Yan, Y. Kim, and S. W. Kim, Coexistence of Surface Superconducting and Three-Dimensional Topological Dirac States in Semimetal KZnBi, Phys. Rev. X **11**, 021065 (2021).

[26] S. Teknowijoyo, N. H. Jo, M. S. Scheurer, M. A. Tanatar, K. Cho, S. L. Bud'ko, P. P. Orth, P. C. Canfield, and R. Prozorov, Nodeless superconductivity in the type-ii dDirac semimetal $PdTe_2$: London penetration depth and pairing-symmetry analysis, Phys. Rev. B **98**, 024508 (2018).

[27] Amit and Y. Singh, Heat capacity evidence for conventional superconductivity in the type-ii dirac semimetal $PdTe_2$, Phys. Rev. B **97**, 054515 (2018).

[28] K. Huang, A. Y. Luo, C. Chen, G. N. Zhang, X. L. Liu, Y. W. Li, F. Wu, S. T. Cui, Z. Sun, C. Jozwiak, A. Bostwick, E. Rotenberg, H. F. Yang, L. X. Yang, G. Xu, Y. F. Guo, Z. K. Liu, and Y. L. Chen, Observation of topological dirac fermions and surface states in superconducting $BaSn_3$, Phys. Rev. B **103**, 155148 (2021).

[29] S. Kobayashi and M. Sato, Topological Superconductivity in Dirac Semimetals, Phys. Rev. Lett. **115**, 187001 (2015).

[30] T. Hashimoto, S. Kobayashi, Y. Tanaka, and M. Sato, Superconductivity in doped Dirac semimetals, Phys. Rev. B **94**, 014510 (2016).

[31] M. Sato and Y. Ando, Topological superconductors: A review, Rep. Prog. Phys. **80**, 076501 (2017).

[32] J. Alicea, New directions in the pursuit of Majorana fermions in solid state systems, Rep. Prog. Phys. **75**, 076501 (2012).

[33] A. Kitaev, Fault-tolerant quantum computation by anyons, Ann. Phys. **303**, 2 (2003).

[34] S. D. Sarma, M. Freedman, and C. Nayak, Majorana zero modes and topological quantum computation, npj Quantum Inf. **1**, 15001 (2015).

[35] A. Kreisel, P. J. Hirschfeld, and B. M. Andersen, On the remarkable superconductivity of fese and its close cousins, Symmetry **12**, 1402 (2020).

[36] L. Kong, L. Cao, S. Zhu, M. Papaj, G. Dai, G. Li, P. Fan, W. Liu, F. Yang, X. Wang, S. Du, C. Jin, L. Fu, H.-J. Gao, and H. Ding, Majorana zero modes in impurity-assisted vortex of lifeas superconductor, Nat. Commun. **12**, 4146 (2021).

[37] P. E. Blöchl, Projector augmented-wave method, Phys. Rev. B **50**, 17953 (1994).

[38] J. P. Perdew, K. Burke, and M. Ernzerhof, Generalized Gradient Approximation Made Simple, Phys. Rev. Lett. **77**, 3865 (1996).

[39] G. Kresse and D. Joubert, From ultrasoft pseudopotentials to the projector augmented-wave method, Phys. Rev. B **59**, 1758 (1999).

[40] A. A. Soluyanov and D. Vanderbilt, Wannier representation of $\mathbb{z}_2$ topological insulators, Phys. Rev. B **83**, 035108 (2011).

[41] Q. Wu, S. Zhang, H.-F. Song, M. Troyer, and A. A. Soluyanov, Wanniertools: An open-source software package for novel topological materials, Comput. Phys. Commun. **224**, 405 (2018).

[42] N. Marzari, A. A. Mostofi, J. R. Yates, I. Souza, and D. Vanderbilt, Maximally localized Wannier functions: Theory and applications, Rev. Mod. Phys. **84**, 1419 (2012).

[43] P. Giannozzi Jr., O. Andreussi, T. Brumme, O. Bunau, M. B. Nardelli, M. Calandra, R. Car, C. Cavazzoni, D. Ceresoli, M. Cococcioni, N. Colonna, I. Carnimeo, A. D. Corso, S. de Gironcoli, P. Delugas, R. A. D. Jr, A. Ferretti, A. Floris, G. Fratesi, G. Fugallo *et al.*, Advanced capabilities for materials modelling with quantum espresso, J. Phys.: Condens. Matter **29**, 465901 (2017).

[44] J. W. Villanova, E. Barnes, and K. Park, Engineering and probing topological properties of Dirac semimetal films by asymmetric charge transfer, Nano Lett. **17**, 963 (2017).

[45] S. M. Young, S. Chowdhury, E. J. Walter, E. J. Mele, C. L. Kane, and A. M. Rappe, Theoretical investigation of the evolution of the topological phase of bi_2se_3 under mechanical strain, Phys. Rev. B **84**, 085106 (2011).

[46] M. S. Bahramy, B.-J. Yang, R. Arita, and N. Nagaosa, Emergence of non-centrosymmetric topological insulating phase in BiTeI under pressure, Nat. Commun. **3**, 679 (2012).

[47] A. Bansil, H. Lin, and T. Das, *Colloquium*: Topological band theory, Rev. Mod. Phys. **88**, 021004 (2016).

[48] T. Ideue, M. Hirayama, H. Taiko, T. Takahashi, M. Murase, T. Miyake, S. Murakami, T. Sasagawa, and Y. Iwasa, Pressure-induced topological phase transition in noncentrosymmetric elemental tellurium, Proc. Natl. Acad. Sci. **116**, 25530 (2019).

[49] P. J. W. Moll, N. L. Nair, T. Helm, A. C. Potter, I. Kimchi, A. Vishwanath, and J. G. Analytis, Transport evidence for fermi-arc-mediated chirality transfer in the dirac semimetal Cd_3As_2, Nature (London) **535**, 266 (2016).

[50] A. A. Burkov, M. D. Hook, and L. Balents, Topological nodal semimetals, Phys. Rev. B **84**, 235126 (2011).

[51] J. Xiong, S. K. Kushwaha, T. Liang, J. W. Krizan, M. Hirschberger, W. Wang, R. J. Cava, and N. P. Ong, Evidence for the chiral anomaly in the dirac semimetal Na_3Bi, Science **350**, 413 (2015).

[52] Z. Jia, C. Li, X. Li, J. Shi, Z. Liao, D. Yu, and X. Wu, Thermoelectric signature of the chiral anomaly in Cd_3As_2, Nat. Commun. **7**, 13013 (2016).

[53] A. A. Burkov, Giant planar Hall effect in topological metals, Phys. Rev. B **96**, 041110(R) (2017).

[54] M. Wu, G. Zheng, W. Chu, Y. Liu, W. Gao, H. Zhang, J. Lu, Y. Han, J. Zhou, W. Ning, and M. Tian, Probing the chiral anomaly by planar hall effect in Dirac semimetal Cd_3As_2 nanoplates, Phys. Rev. B **98**, 161110(R) (2018).

[55] G. Pizzi, V. Vitale, R. Arita, S. Blügel, F. Freimuth, G. Géranton, M. Gibertini, D. Gresch, C. Johnson, T. Koretsune, J. Ibañez-Azpiroz, H. Lee, J.-M. Lihm, D. Marchand, A. Marrazzo, Y. Mokrousov, J. I. Mustafa, Y. Nohara, Y. Nomura, L. Paulatto *et al.*, Wannier90 as a community code: New features and applications, J. Phys.: Condens. Matter **32**, 165902 (2020).